PERGAMON

Available online at www.sciencedirect.com

SCIENCE DIRECT®

International Journal of Heat and Mass Transfer 46 (2003) 1653–1663

International Journal of HEAT and MASS TRANSFER

www.elsevier.com/locate/ijhmt

3D modeling of evaporation of water injected into a plasma jet

Kandasamy Ramachandran, Takehiko Sato, Hideya Nishiyama *

Institute of Fluid Science, Tohoku University, 2-1-1, Katahira, Aoba-ku, Sendai 980-8577, Japan

Received 7 January 2002; received in revised form 22 July 2002

Abstract

3D effects of the radial injection of water jet into the swirl and non-swirl plasma jets are clarified numerically. The plasma–droplet two-way interactions are modeled by coupling Lagrangian approach for droplet behavior with an Eulerian approach for plasma flow under the dense loading. The effect of radial injection of the water jet on the temperature and flow fields of the swirl and non-swirl plasma jets is studied numerically. Mass concentration of the evaporated vapor is also predicted. The local deformation of the thermo-fluid fields of the plasma jet is stronger for higher droplet loading. Evaporation rate is decreased with increasing the droplet loading as well as swirl velocity. Mixing of vapor with plasma is stronger in the presence of swirl.

1. Introduction

Liquid feedstock has been used for thermal plasma synthesis of new materials [1,2], production of nanoparticles [3,4] and waste treatment [5,6]. In these processes, liquid feedstock material undergoes evaporation, decomposition and ionization. Hence understanding of complex plasma–droplet interactions is very important to optimize the process parameters and control the process. Many works have been published on plasma–particle interactions, which are applicable to plasma spraying e.g. [7–9]. Wan et al. [10] have reviewed these works and compared the results of heat and diffusion controlled evaporation models. Only few papers have been published on the droplet interactions with plasma by injecting liquid feedstock. Paik et al. [11] have presented some numerical results of water droplet trajectories in the counterflow plasma reactor in their paper. Kolman et al. [12] have developed three dimensional two-phase model for thermal plasma chemical vapor deposition with liquid feedstock injection. Their work is mainly focused on CVD deposition of diamond. In order to understand the behavior of the droplets in the plasma jet, Wittmann et al. [13] have studied the interaction of water jet with DC plasma jet by optical emission spectroscopy.

With this in mind, we develop a 3D model, which includes the diffusion controlled evaporation, turbulent mixing of vapor with plasma and further some effects of droplet loading, swirl velocity and evaporation, to study the effect of transverse injection of water droplet jet on the plasma thermo-fluid fields and droplet behavior in the plasma jet.

2. Mathematical model

The following assumptions are introduced in this model:

1. The plasma is continuous and in local thermodynamic equilibrium.
2. The plasma is optically thin.

* Corresponding author. Fax: +81-22-217-5261.
E-mail address: nishiyama@ifs.tohoku.ac.jp (H. Nishiyama).

0017-9310/03/$ - see front matter © 2002 Published by Elsevier Science Ltd.
PII: S0017-9310(02)00440-4

Nomenclature

Plasma jet model

c_1, c_2	constant in K–ε model
C_p	specific heat capacity at constant pressure, $\mathrm{J\,kg^{-1}\,K^{-1}}$
$C_\mu C_D$	constant in K–ε model
h	enthalpy, $\mathrm{J\,kg^{-1}}$
K	turbulent kinetic energy, $\mathrm{J\,kg^{-1}}$
k	thermal conductivity, $\mathrm{W\,m^{-1}\,K^{-1}}$
m	constant used in temperature input profile
n	constant used in axial velocity input profile
P	pressure, Pa
Pr	Prandtl or Schmidt number
r	radial distance, m
R_0	radius of the nozzle exit, m
S	source term
T	temperature, K
u	azimuthal velocity, $\mathrm{m\,s^{-1}}$
v	radial velocity, $\mathrm{m\,s^{-1}}$
w	axial velocity, $\mathrm{m\,s^{-1}}$
x	azimuthal distance in figures, m
y	radial distance in figures, m
x	mole fraction
y	mass fraction
z	axial distance, m
θ	azimuthal distance, rad
Γ	exchange coefficient
ρ	density, $\mathrm{kg\,m^{-3}}$
ν	kinematic viscosity, $\mathrm{m^2\,s^{-1}}$
μ	dynamic viscosity, $\mathrm{kg\,m^{-1}\,s^{-1}}$
ε	dissipation rate, $\mathrm{J\,kg^{-1}\,s^{-1}}$
σ	constant in K–ε model

Subscripts

l	laminar
max	maximum
dh	droplet enthalpy
dm	droplet momentum
dM	droplet mass
Ra	radiation
t	turbulent

Plasma–droplet interactions model

a	thermal accommodation coefficient
B_M	mass transfer number
C_{Df}	corrected drag coefficient
C_p	specific heat capacity at constant pressure, $\mathrm{J\,kg^{-1}\,K^{-1}}$
d	diameter, m
f	correction factor
g	gravitation constant, $\mathrm{m\,s^{-2}}$
h	enthalpy, $\mathrm{J\,kg^{-1}}$
k	thermal conductivity, $\mathrm{W\,m^{-1}\,K^{-1}}$
L	latent heat of evaporation, $\mathrm{J\,kg^{-1}}$
M	mass, kg
P	total pressure of the plasma gas, Pa
P_{vp}	partial pressure of the vapor at the surface of the droplet, Pa
Pr	Prandtl number,
Re_d	droplet Reynolds number, $d_p\lvert\vec{U}_g - \vec{U}_d\rvert/\nu$
T	temperature, K
t	time, s
$\vec{U}$	mean velocity, $\mathrm{m\,s^{-1}}$
V	volume, $\mathrm{m^3}$
W	molecular weight, $\mathrm{kg\,mol^{-1}}$
$\vec{X}$	droplet displacement, m
y	mass fraction
ρ	density, $\mathrm{kg\ m^{-3}}$
η	number flow rate of the particles, $\mathrm{s^{-1}}$
μ	dynamic viscosity, $\mathrm{kg\,m^{-1}\,s^{-1}}$
γ	specific heat ratio of gas, C_p/C_v

Subscripts

d	droplet
dh	droplet enthalpy
dm	droplet momentum
dM	droplet mass
f	value calculated at the film temperature
g	gas (plasma)
s	surface of the droplet
vp	vapor
vps	vapor at the surface of the droplet
vpg	vapor in the plasma gas surrounding the droplet

Superscripts

0	at the start of Lagrangian time step
n	at the end of Lagrangian time step

3. The plasma flow is steady, turbulent, non-reactive and incompressible.
4. Swirl velocity of the plasma jet is given at the nozzle exit.
5. Droplet loading is dense and two-way coupling between the plasma and droplets is considered.
6. Turbulence dispersion of the droplets is neglected but turbulent diffusion of evaporated vapor is included.

2.1. Plasma jet model

The governing equations to simulate the plasma jet flow are as follows:

Equation of continuity

$$\frac{1}{r}\frac{\partial}{\partial\theta}(\rho u) + \frac{1}{r}\frac{\partial}{\partial r}(r\rho v) + \frac{\partial}{\partial z}(\rho w) = S_{dM} \qquad (1)$$

Equation of momentum

Azimuthal

$$\frac{1}{r^2}\frac{\partial}{\partial\theta}(r\rho u^2)+\frac{1}{r}\frac{\partial}{\partial r}(r\rho vu)+\frac{1}{r}\frac{\partial}{\partial z}(r\rho wu)$$
$$=\frac{2}{r}\frac{\partial}{\partial\theta}\left(\Gamma_u\left[\frac{1}{r}\frac{\partial u}{\partial\theta}+\frac{v}{r}\right]\right)+\frac{\partial}{\partial r}\left(\Gamma_u\left[\frac{\partial u}{\partial r}-\frac{u}{r}+\frac{1}{r}\frac{\partial v}{\partial\theta}\right]\right)$$
$$+\frac{\partial}{\partial z}\left(\Gamma_u\left[\frac{\partial u}{\partial z}+\frac{1}{r}\frac{\partial w}{\partial\theta}\right]\right)+\frac{2\Gamma_u}{r}\left(\frac{1}{r}\frac{\partial v}{\partial\theta}+\frac{\partial u}{\partial r}-\frac{u}{r}\right)$$
$$-\frac{\rho vu}{r}-\frac{1}{r}\frac{\partial P}{\partial\theta}+(S_{\mathrm{dm}})_\theta \quad (2)$$

Radial

$$\frac{1}{r^2}\frac{\partial}{\partial\theta}(r\rho uv)+\frac{1}{r}\frac{\partial}{\partial r}(r\rho v^2)+\frac{1}{r}\frac{\partial}{\partial z}(r\rho wv)$$
$$=\frac{1}{r}\frac{\partial}{\partial\theta}\left(\Gamma_v\left[\frac{1}{r}\frac{\partial v}{\partial\theta}+\frac{\partial u}{\partial r}-\frac{u}{r}\right]\right)+2\frac{\partial}{\partial r}\left(\Gamma_v\frac{\partial v}{\partial r}\right)$$
$$+\frac{\partial}{\partial z}\left(\Gamma_v\left[\frac{\partial v}{\partial z}+\frac{\partial w}{\partial r}\right]\right)+\frac{2\Gamma_v}{r}\left[\frac{\partial v}{\partial r}-\frac{1}{r}\frac{\partial u}{\partial\theta}-\frac{v}{r}\right]$$
$$+\frac{\rho u^2}{r}-\frac{\partial P}{\partial r}+(S_{\mathrm{dm}})_r \quad (3)$$

Axial

$$\frac{1}{r^2}\frac{\partial}{\partial\theta}(r\rho uw)+\frac{1}{r}\frac{\partial}{\partial r}(r\rho vw)+\frac{1}{r}\frac{\partial}{\partial z}(r\rho w^2)$$
$$=\frac{1}{r}\frac{\partial}{\partial\theta}\left(\Gamma_w\left[\frac{1}{r}\frac{\partial w}{\partial\theta}+\frac{\partial u}{\partial z}\right]\right)+\frac{1}{r}\frac{\partial}{\partial r}\left(r\Gamma_w\left[\frac{\partial w}{\partial r}+\frac{\partial v}{\partial z}\right]\right)$$
$$+2\frac{\partial}{\partial z}\left(\Gamma_w\frac{\partial w}{\partial z}\right)-\frac{\partial P}{\partial z}+(S_{\mathrm{dm}})_z \quad (4)$$

Equation of energy

$$\frac{1}{r^2}\frac{\partial}{\partial\theta}(r\rho uh)+\frac{1}{r}\frac{\partial}{\partial r}(r\rho vh)+\frac{1}{r}\frac{\partial}{\partial z}(r\rho wh)$$
$$=\frac{1}{r}\frac{\partial}{\partial\theta}\left(\frac{\Gamma_h}{r}\frac{\partial h}{\partial\theta}\right)+\frac{1}{r}\frac{\partial}{\partial r}\left(r\Gamma_h\frac{\partial h}{\partial r}\right)+\frac{\partial}{\partial z}\left(\Gamma_h\frac{\partial h}{\partial z}\right)$$
$$+S_{\mathrm{dh}}-S_{\mathrm{Ra}} \quad (5)$$

Equation of mass fraction of water vapor

$$\frac{1}{r^2}\frac{\partial}{\partial\theta}(r\rho uy_{\mathrm{vp}})+\frac{1}{r}\frac{\partial}{\partial r}(r\rho vy_{\mathrm{vp}})+\frac{1}{r}\frac{\partial}{\partial z}(r\rho wy_{\mathrm{vp}})$$
$$=\frac{1}{r}\frac{\partial}{\partial\theta}\left(\frac{\Gamma_{\mathrm{vp}}}{r}\frac{\partial y_{\mathrm{vp}}}{\partial\theta}\right)+\frac{1}{r}\frac{\partial}{\partial r}\left(r\Gamma_{\mathrm{vp}}\frac{\partial y_{\mathrm{vp}}}{\partial r}\right)$$
$$+\frac{\partial}{\partial z}\left(\Gamma_{\mathrm{vp}}\frac{\partial y_{\mathrm{vp}}}{\partial z}\right)+S_{\mathrm{dM}} \quad (6)$$

The standard K–ε model is used to take into account the turbulent characteristics of the jet. The turbulent kinetic energy and its dissipation rate equations are

$$\frac{1}{r^2}\frac{\partial}{\partial\theta}(r\rho uK)+\frac{1}{r}\frac{\partial}{\partial r}(r\rho vK)+\frac{1}{r}\frac{\partial}{\partial z}(r\rho wK)$$
$$=\frac{1}{r}\frac{\partial}{\partial\theta}\left(\frac{\Gamma_K}{r}\frac{\partial K}{\partial\theta}\right)+\frac{1}{r}\frac{\partial}{\partial r}\left(r\Gamma_K\frac{\partial K}{\partial r}\right)$$
$$+\frac{\partial}{\partial z}\left(\Gamma_K\frac{\partial K}{\partial z}\right)+G-\rho\varepsilon \quad (7)$$

$$\frac{1}{r^2}\frac{\partial}{\partial\theta}(r\rho u\varepsilon)+\frac{1}{r}\frac{\partial}{\partial r}(r\rho v\varepsilon)+\frac{1}{r}\frac{\partial}{\partial z}(r\rho w\varepsilon)$$
$$=\frac{1}{r}\frac{\partial}{\partial\theta}\left(\frac{\Gamma_\varepsilon}{r}\frac{\partial\varepsilon}{\partial\theta}\right)+\frac{1}{r}\frac{\partial}{\partial r}\left(r\Gamma_\varepsilon\frac{\partial\varepsilon}{\partial r}\right)+\frac{\partial}{\partial z}\left(\Gamma_\varepsilon\frac{\partial\varepsilon}{\partial z}\right)$$
$$+\frac{\varepsilon}{K}(c_1G-c_2\rho\varepsilon) \quad (8)$$

where

$$G=\rho\nu_{\mathrm{t}}\left\{2\left[\left(\frac{\partial w}{\partial z}\right)^2+\left(\frac{\partial v}{\partial r}\right)^2+\left(\frac{1}{r}\frac{\partial u}{\partial\theta}+\frac{v}{r}\right)^2\right]\right.$$
$$+\left(\frac{\partial w}{\partial r}+\frac{\partial v}{\partial z}\right)^2+\left(\frac{\partial u}{\partial z}+\frac{1}{r}\frac{\partial w}{\partial\theta}\right)^2$$
$$\left.+\left(\frac{1}{r}\frac{\partial v}{\partial\theta}+\frac{\partial u}{\partial r}-\frac{u}{r}\right)^2\right\} \quad (9)$$

S_{Ra} is a source term for radiative losses of the plasma only. The terms S_{dM}, S_{dm} and S_{dh} are described in the next section. The diffusion coefficients are given as

$$\Gamma_u=\Gamma_v=\Gamma_w=\rho(\nu_1+\nu_{\mathrm{t}});$$
$$\Gamma_h=\Gamma_{\mathrm{vp}}=\rho(\nu_1/Pr_1+\nu_{\mathrm{t}}/Pr_{\mathrm{t}}) \quad (10)$$

$$\Gamma_K=\rho(\nu_1+\nu_{\mathrm{t}}/\sigma_K);\quad \Gamma_\varepsilon=\rho(\nu_1+\nu_{\mathrm{t}}/\sigma_\varepsilon) \quad (11)$$

and turbulent kinematic viscosity (ν_{t}) is determined by

$$\nu_{\mathrm{t}}=C_\mu C_D K^2/\varepsilon \quad (12)$$

where constants, c_1, c_2, $C_\mu C_D$, Pr_{t}, σ_K, σ_ε are 1.44, 1.92, 0.09, 0.7, 1.0 and 1.3 respectively [14].

The temperature-dependent (300–24,000 K) transport and thermodynamic properties of Ar [15] and water vapor [16] are used for the present calculations. The simple mixing rule [17] adopted to account for the mixing of the water vapor (vp) into the Ar plasma jet is given by

$$h=y_{\mathrm{Ar}}h_{\mathrm{Ar}}+y_{\mathrm{vp}}h_{\mathrm{vp}} \quad (13)$$

$$1/\rho=y_{\mathrm{Ar}}/\rho_{\mathrm{Ar}}+y_{\mathrm{vp}}/\rho_{\mathrm{vp}} \quad (14)$$

$$C_{\mathrm{p}}=y_{\mathrm{Ar}}C_{\mathrm{p_{Ar}}}+y_{\mathrm{vp}}C_{\mathrm{pvp}} \quad (15)$$

$$\mu=x_{\mathrm{Ar}}\mu_{\mathrm{Ar}}+x_{\mathrm{vp}}\mu_{\mathrm{vp}} \quad (16)$$

$$k=x_{\mathrm{Ar}}k_{\mathrm{Ar}}+x_{\mathrm{vp}}k_{\mathrm{vp}} \quad (17)$$

Fig. 1(a) and (b) show the schematic illustration of the computational model and computational domain with grids respectively to simulate the 3D droplet-laden

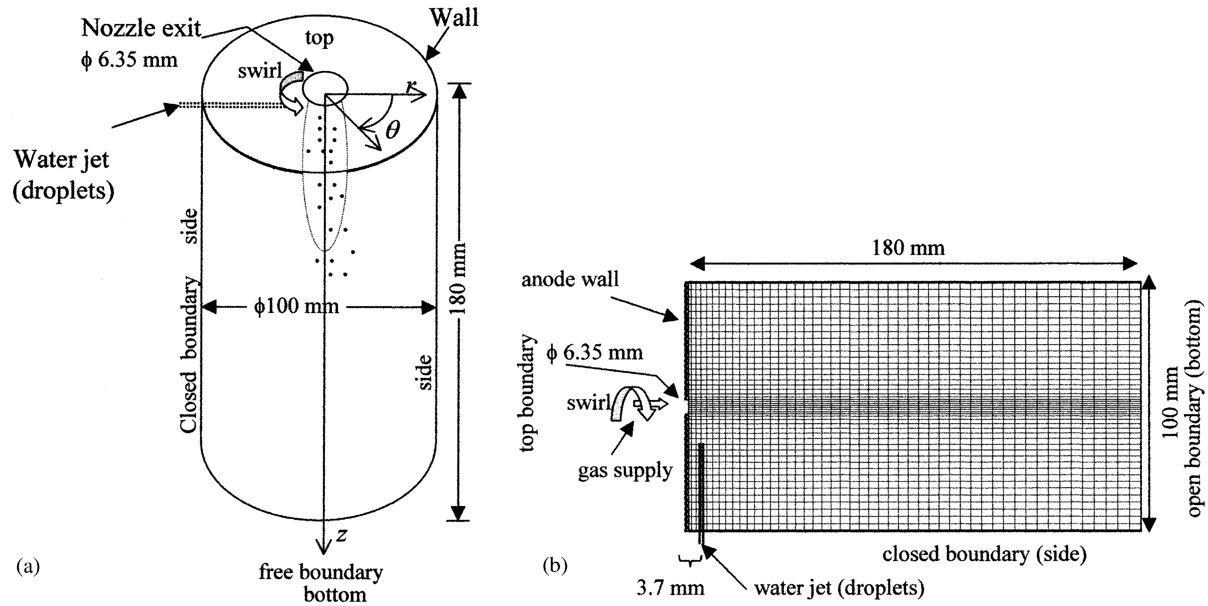

Fig. 1. (a) Schematic diagram of the computational model and (b) computational domain with grids.

plasma jet. The size of the computational domain used for the calculation is 100, 180 mm, and 2π radians in the radial, axial, and azimuthal directions, respectively. The number of grid points in the computational domain is 48,000 ($40 \times 24 \times 50$). Non-uniform mesh size is adopted in radial and axial directions. But uniform mesh size is adopted in the central region (in radial direction) and in azimuthal direction. The bottom and side boundaries are free and closed respectively. The nozzle exit diameter is 6.35 mm at the top boundary while the remaining top boundary is set to be a wall. Known values of the temperature, axial and azimuthal velocities, turbulent kinetic energy and dissipation rate at the nozzle exit are given as the nozzle exit boundary values. The solid vortex swirl velocity [18] and parabolic [19] axial velocity and temperature profiles at the nozzle exit are assumed to be

$$u = u_{\max}(r/R_0) \tag{18}$$

$$w = w_{\max}[1 - (r/R_0)^n] \tag{19a}$$

$$T = (T_{\max} - T_{\text{wall}})[1 - (r/R_0)^m] + T_{\text{wall}} \tag{19b}$$

where $u_{\max}$, T_{wall}, n and m are set to 20 or 40 m s^{-1}, 500 K, 2.0 and 2.0 respectively. The values of $T_{\max}$ and $w_{\max}$, calculated from the experimental conditions [20], are 9125 K, and 427 m s^{-1} respectively. Swirl numbers are 0.045 and 0.09 respectively for maximum swirl velocities ($u_{\max}$) 20 and 40 m s^{-1} at the nozzle exit. Since the radial velocity is negligible compared with axial velocity, it is not given here.

2.2. Plasma–droplet interactions model

Lagrangian method, which describes the evolution of position, velocity, and temperature of the water droplet, is used to simulate the droplet behavior in the plasma jet. The position of the droplet is determined from its velocity as

$$\frac{\mathrm{d}\vec{X}_\mathrm{d}}{\mathrm{d}t} = \vec{U}_\mathrm{d} \tag{20}$$

where $\vec{U}_\mathrm{d}$ is calculated by

$$M_\mathrm{d}\frac{\mathrm{d}\vec{U}_\mathrm{d}}{\mathrm{d}t} = D_\mathrm{d}(\vec{U}_\mathrm{g} - \vec{U}_\mathrm{d}) + M_\mathrm{d}\vec{g}\left(1 - \frac{\rho_\mathrm{g}}{\rho_\mathrm{d}}\right) - V_\mathrm{d}\nabla P \tag{21}$$

The drag coefficient, droplet projected area, and density of the plasma are used to evaluate the drag function, D_d as

$$D_\mathrm{d} = \tfrac{1}{2}\rho_\mathrm{g}A_\mathrm{d}C_\mathrm{Df}|\vec{U}_\mathrm{g} - \vec{U}_\mathrm{d}| \tag{22}$$

where C_Df is calculated by [10,12]

$$C_\mathrm{Df} = \left(\frac{24}{Re_\mathrm{d}} + \frac{6}{1+\sqrt{Re_\mathrm{d}}} + 0.4\right)f_1^{-0.45}f_2^{0.45}f_3 \tag{23}$$

The correction factors f_1, f_2 and f_3 can be obtained by

$$f_1 = \frac{\rho_\mathrm{g}\mu_\mathrm{g}}{\rho_\mathrm{s}\mu_\mathrm{s}} \tag{24a}$$

$$f_2 = \left[1 + \left(\frac{2-a}{a}\right)\left(\frac{\gamma_\mathrm{s}}{1+\gamma_\mathrm{s}}\right)\frac{4}{Pr_\mathrm{s}}Kn\right]^{-1} \tag{24b}$$

$$f_3 = \frac{1}{B_{\mathrm{M}}}\ln(1 + B_{\mathrm{M}}) \tag{24c}$$

where

$$Kn = \frac{2Pr_{\mathrm{s}}k_{\mathrm{f}}}{\rho_{\mathrm{gs}}\lambda d_{\mathrm{d}}C_{\mathrm{pf}}} \quad \text{and} \quad \lambda = \left(\frac{8\mathrm{R}T_{\mathrm{s}}}{\pi W}\right)^{1/2} \tag{25a}$$

$$B_{\mathrm{M}} = \left[\frac{y_{\mathrm{vps}} - y_{\mathrm{vpg}}}{1 - y_{\mathrm{vps}}}\right] \quad \text{and}$$

$$y_{\mathrm{vps}} = \left[1 + \left(\frac{P}{P_{\mathrm{vp}}} - 1\right)\frac{W_{\mathrm{g}}}{W_{\mathrm{vp}}}\right]^{-1} \tag{25b}$$

Now, droplet projected area (A_{d}) and volume (V_{d}) are given by

$$A_{\mathrm{d}} = \frac{\pi d_{\mathrm{d}}^2}{4} \tag{26}$$

and

$$V_{\mathrm{d}} = \frac{\pi d_{\mathrm{d}}^3}{6} \tag{27}$$

The temperature of the droplet is determined from the solution of the heat balance equation neglecting the radiation effect

$$M_{\mathrm{d}}C_{\mathrm{pd}}\frac{\mathrm{d}T_{\mathrm{d}}}{\mathrm{d}t} = L_{\mathrm{d}}\frac{\mathrm{d}M_{\mathrm{d}}}{\mathrm{d}t} + \alpha(T_{\mathrm{g}} - T_{\mathrm{d}}) \tag{28}$$

The evolution of the mass of the droplet, M_{d} is described by droplet mass equation as

$$\frac{\mathrm{d}M_{\mathrm{d}}}{\mathrm{d}t} = -\pi d_{\mathrm{d}}\left(\frac{k_{\mathrm{vp}}}{C_{\mathrm{pvp}}}\right)_{\mathrm{f}} Nu_1 \ln(1 + B_{\mathrm{M}}) \tag{29}$$

and α is calculated by

$$\alpha = \pi k_{\mathrm{f}} Nu_2 d_{\mathrm{d}} \tag{30}$$

where the Nusselt numbers Nu_1 and Nu_2 are obtained from the droplet Reynolds number and the Prandtl number as [10,12]

$$Nu_1 = 2\left(1 + 0.3\sqrt{Re_{\mathrm{d}}}Pr^{1/3}\right)\left(\frac{C_{\mathrm{pg}}}{C_{\mathrm{ps}}}\right)^{0.38} f_1^{0.6} \tag{31a}$$

$$Nu_2 = 2\left(1 + 0.3\sqrt{Re_{\mathrm{d}}}Pr^{1/3}\right)\left(\frac{C_{\mathrm{pg}}}{C_{\mathrm{ps}}}\right)^{0.38} f_1^{0.6} f_2 f_3 \tag{31b}$$

The correction factors f_1, f_2 and f_3 are given in Eqs. ((24a)–(24c)).

The droplet source terms, included in the governing Eqs. ((1)–(6)) by using PSI-CELL technique [21], which account for the exchange of mass (S_{dM}), momentum (S_{dm}) and energy (S_{dh}) between the plasma and droplet, are given by

$$S_{\mathrm{dM}} = \frac{\pi}{6}\sum \eta\left[\rho_{\mathrm{d}}^0(d_{\mathrm{d}}^0)^3 - \rho_{\mathrm{d}}^n(d_{\mathrm{d}}^n)^3\right] \tag{32}$$

$$S_{\mathrm{dm}} = \frac{\pi}{6}\sum \eta\left[\rho_{\mathrm{d}}^0\vec{U}_{\mathrm{d}}^0(d_{\mathrm{d}}^0)^3 - \rho_{\mathrm{d}}^n\vec{U}_{\mathrm{d}}^n(d_{\mathrm{d}}^n)^3\right] \tag{33}$$

$$S_{\mathrm{dh}} = \frac{\pi}{6}\sum \eta\left[\rho_{\mathrm{d}}^0 h_{\mathrm{d}}^0(d_{\mathrm{d}}^0)^3 - \rho_{\mathrm{d}}^n h_{\mathrm{d}}^n(d_{\mathrm{d}}^n)^3\right] \tag{34}$$

$\sum$ is summation over all of the Lagrangian time steps required for the droplet to traverse the cell and for all droplets.

3. Numerical procedure

The SIMPLEST algorithm is used to solve the Eqs. ((1)–(8)) through PHOENICS CFD code [22]. The droplet size and injection velocity are assumed as 50 μm (spherical) and 5.0 m s^{-1} (in radial direction) respectively. The injection position is fixed at 6.18 mm away from the axis of symmetry and 3.7 mm below the nozzle exit as shown in Fig 1(b). The maximum droplet loading ratio (mass flow rate of the droplet jet/mass flow rate of the plasma gas) used in this calculation is 0.25. Heat conduction inside the droplet and droplet radiation effect are neglected according to the Refs. [11] and [23]. Since the Basset history term, and thermophoresis have no appreciable influence on particles with a size between 10 and 100 μm [24], they are not considered in this model.

4. Results and discussion

4.1. 3D effects in non-swirl plasma jet

Fig. 2(a) and (b) show the temperature fields of the non-swirl plasma jet for the droplet loading 300 and 600 g/h respectively. The position of the droplet jet is marked by a black dot. The droplet jet penetrates through a core region of the plasma jet. Since the droplet jet takes thermal energy from the surrounding plasma, the local deformation is appeared along the droplet jet trajectory. The local deformation is relaxed in the downstream direction. Strong deformation is noticed at the core region of the plasma jet and for higher droplet loading (600 g/h). This is because high heat transfer at the core region of the plasma jet due to the large temperature difference between plasma and droplet, and the higher mass takes more energy from the plasma. The axial velocity fields of the non-swirl plasma jet are shown for the droplet loading 300 g/h (Fig. 3(a)) and 600 g/h (Fig. 3(b)). Local deformation of velocity fields of plasma is due to momentum exchange between plasma and droplets. The features of the velocity fields are almost similar to that of temperature fields shown in Fig. 2(a) and (b). However, it seems that local deformation of the velocity fields are relaxed slower than that of temperature fields in the downstream direction. Since

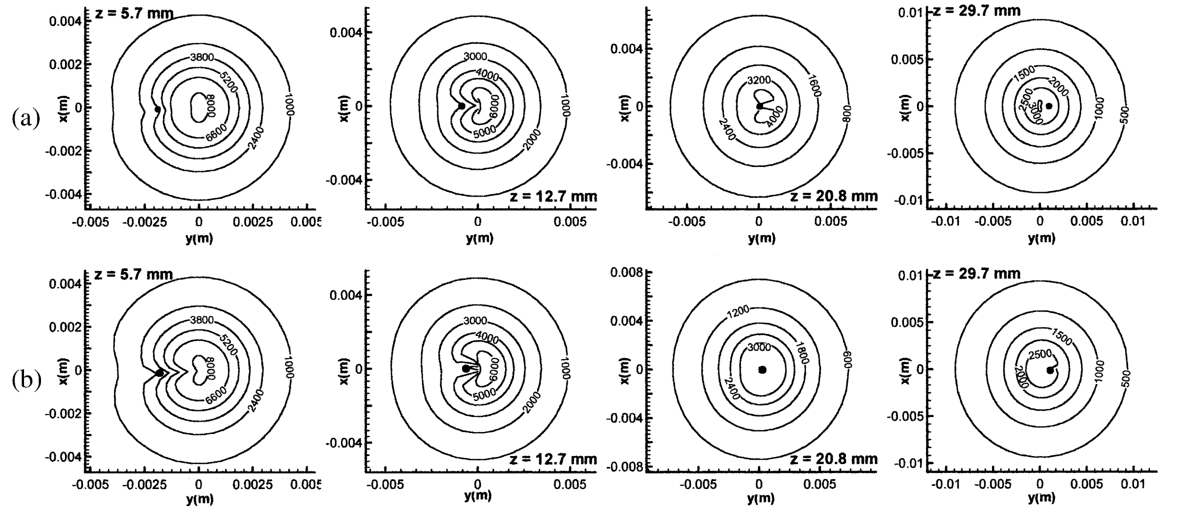

Fig. 2. Effect of droplet loading on temperature field (K) of the non-swirl plasma jet: (a) 300 and (b) 600 g/h.

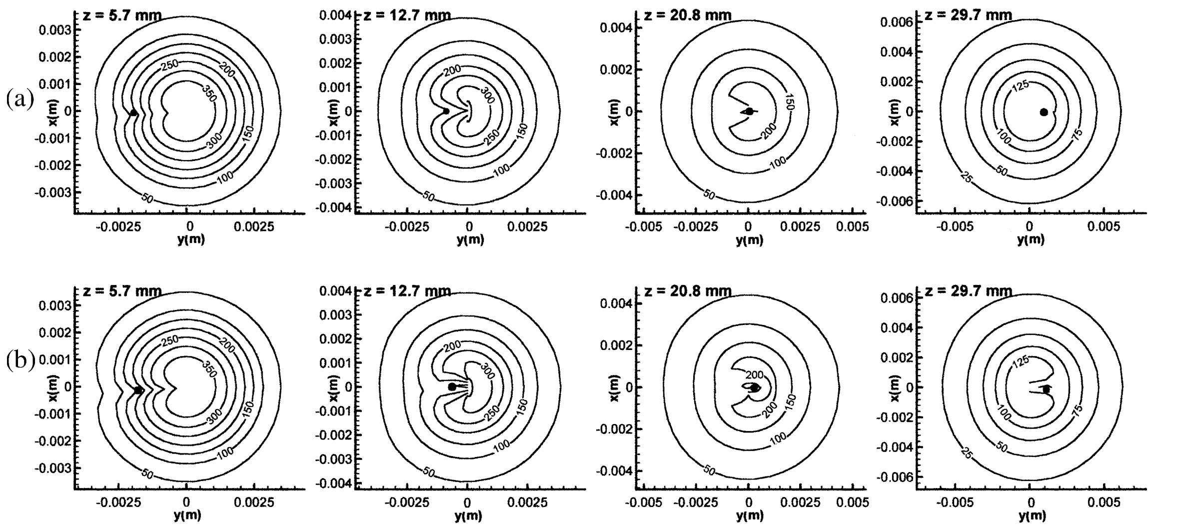

Fig. 3. Effect of droplet loading on axial velocity field ($m\,s^{-1}$) of the non-swirl plasma jet: (a) 300 and (b) 600 g/h.

the evaporation rate is relatively low, we assumed that the effect of jet expansion by droplet evaporation on the plasma jet temperature and velocity is negligible.

Fig. 4(a) and (b) show the vapor mass concentration in the downstream direction for the droplet loading 300 and 600 g/h respectively. Mixing of vapor with plasma is predominant at the backside of the droplet. When the droplet crossing the core region of the plasma jet, maximum mass concentration is achieved. The shape of the vapor mass concentration field is being deformed as the shape of the plasma jet fields in the downstream direction. Also area of the vapor clouds is increased in the same. This indicates that mixing is increased in the downstream direction. The mass concentration of the vapor is higher for higher droplet loading (600 g/h) relative to the lower droplet loading (300 g/h).

4.2. 3D effects in swirl plasma jet

The temperature fields of the swirl plasma jet are shown for the swirl velocity 20 $m\,s^{-1}$ (Fig. 5(a)) and 40 $m\,s^{-1}$ (Fig. 5(b)) at the droplet loading 600 g/h. The deformation of the plasma temperature fields is rotated an anti-clockwise direction. This is because the droplet jet obtains angular momentum from the plasma jet fringe, where the angular momentum is high and travels in the azimuthal direction. The local deformation of the temperature fields is stronger for the swirl velocity 20

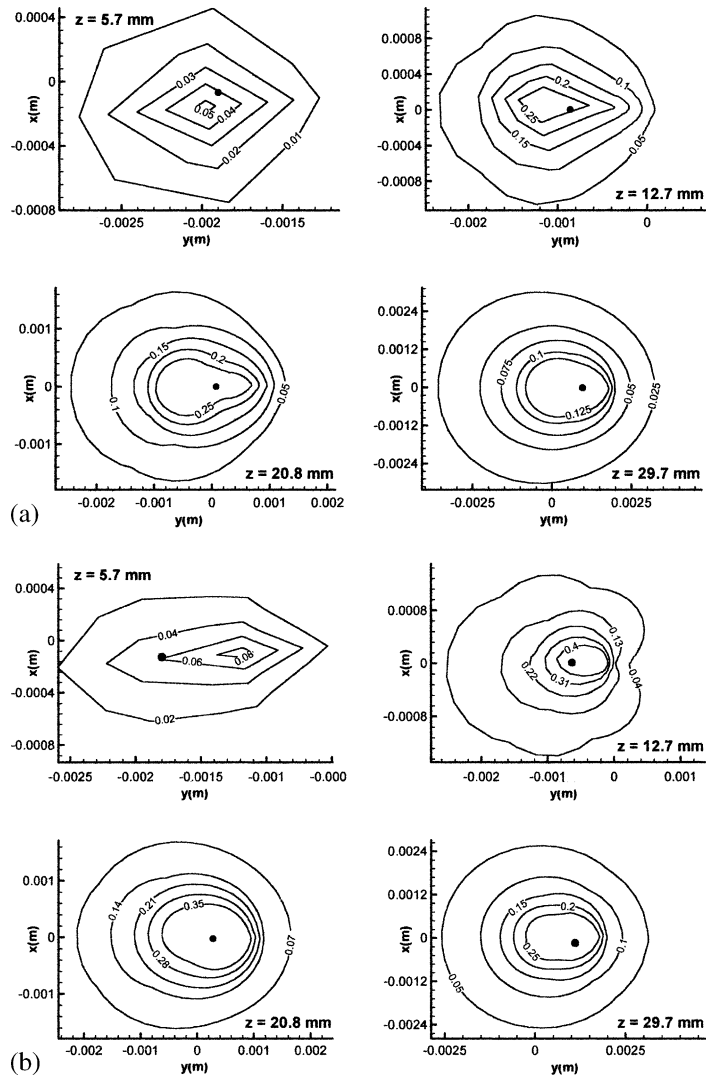

Fig. 4. Vapor mass concentration at different axial locations for different droplet loading: (a) 300 and (b) 600 g/h.

$m\,s^{-1}$ (Fig. 5(a)) compared with the same for the swirl velocity 40 $m\,s^{-1}$ (Fig. 5(b)). Since increasing swirl velocity prevents the droplet jet penetration into the core region of the plasma jet, heat transfer from the plasma to the droplets is decreased with increasing swirl velocity. Fig. 6(a) and (b) shows the axial velocity fields of the swirl plasma jet for the swirl velocity 20 and 40 $m\,s^{-1}$ respectively at the droplet loading 600 g/h. The features of the velocity fields are similar to that of the temperature fields (Fig. 5(a) and (b)). However the local deformation of the velocity fields due to momentum exchange is relaxed slower than that of temperature fields as seen the same in the non-swirl plasma jet.

The vapor mass concentration in the swirl plasma jet is shown for the swirl velocity 20 $m\,s^{-1}$ (Fig. 7(a)) and 40 $m\,s^{-1}$ (Fig. 7(b)) at the droplet loading 600 g/h. The shape and position of the vapor mass concentration fields are differed from the same in Fig. 4(a) and (b). The vapor cloud is rotated in an anti-clockwise direction by swirl velocity. This rotation is stronger for higher swirl velocity (40 $m\,s^{-1}$).

4.3. Droplet evaporation

Variation of the droplet size in the plasma jet for different conditions is shown in Fig. 8. The evaporation rate is increased with decreasing the droplet loading in case of non-swirl jet. The same is decreased with increasing swirl velocity in the case of swirl jet. High swirl velocity (40 $m\,s^{-1}$) and high droplet loading (600 g/h) reduce the evaporation rate significantly. It can be suggested that annular injection with lower droplet loading

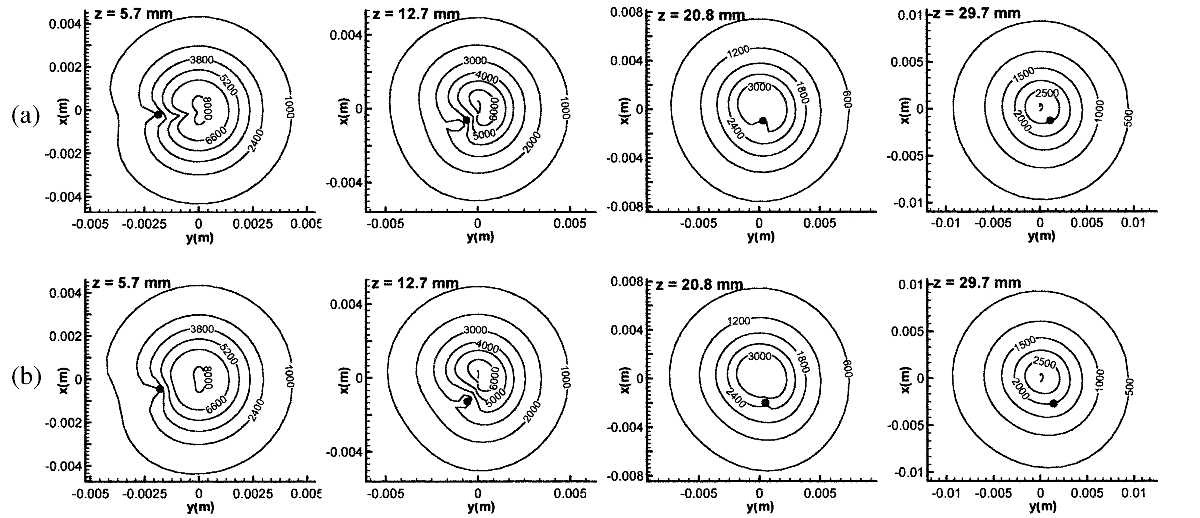

Fig. 5. Temperature field (K) of the swirl plasma jet for different swirl velocities: (a) 20 and (b) 40 $m\,s^{-1}$ (droplet loading = 600 g/h).

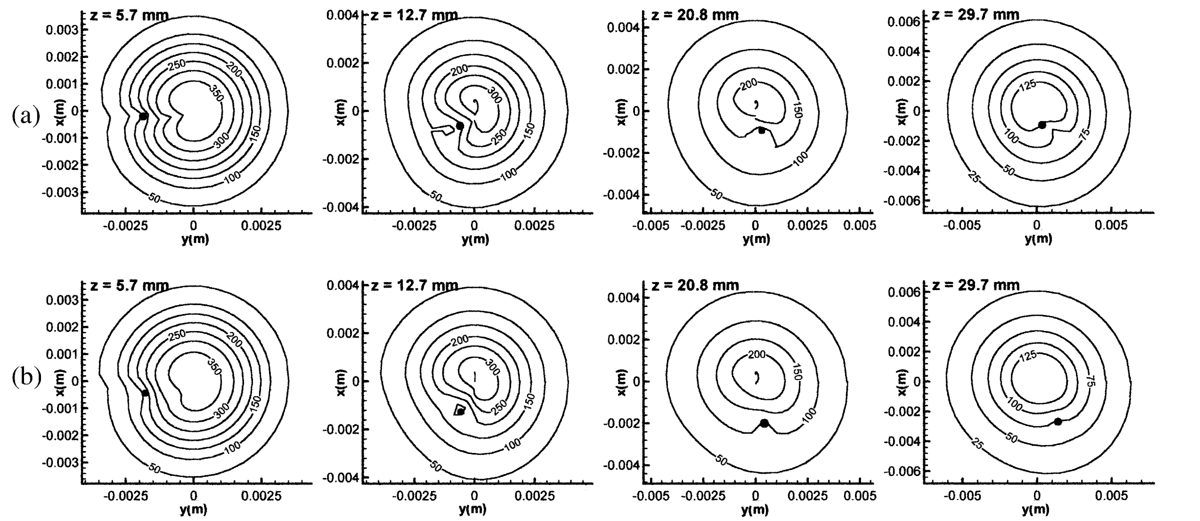

Fig. 6. Influence of the swirl velocity on axial velocity field ($m\,s^{-1}$) of the swirl plasma jet: (a) 20 and (b) 40 $m\,s^{-1}$ (droplet loading 600 g/h).

would be preferred to increase the rate of production and evaporation. In this case the same amount of plasma power is utilized to evaporate higher mass of the droplets.

4.4. Radial distribution of plasma jet temperature and vapor mass concentration

Figs. 9 and 10 show the radial distributions of the plasma temperature and vapor mass concentration at two different axial locations. Fig. 9(a) and (b) drawn for the droplet loading 300 and 600 g/h respectively in the case of non-swirl plasma jet. The water jet shifts the plasma jet axis to the right side and decreases the plasma temperature significantly at $z = 12.7$ mm. The deflection of the curve corresponds to the droplet jet location and results in the plasma temperature decrement near the plasma jet axis. Since higher mass consumes more energy, these effects are stronger for higher droplet loading (600 g/h) relative to the lower droplet loading (300 g/h). The vapor concentration is higher at higher temperature region and for higher droplet loading. However rate of evaporation is lower at higher droplet loading. In the plasma–droplet interactions, the heat from the plasma is utilized to evaporate the droplet as well as to heat-up the vapor around the droplet. In addition to the droplet

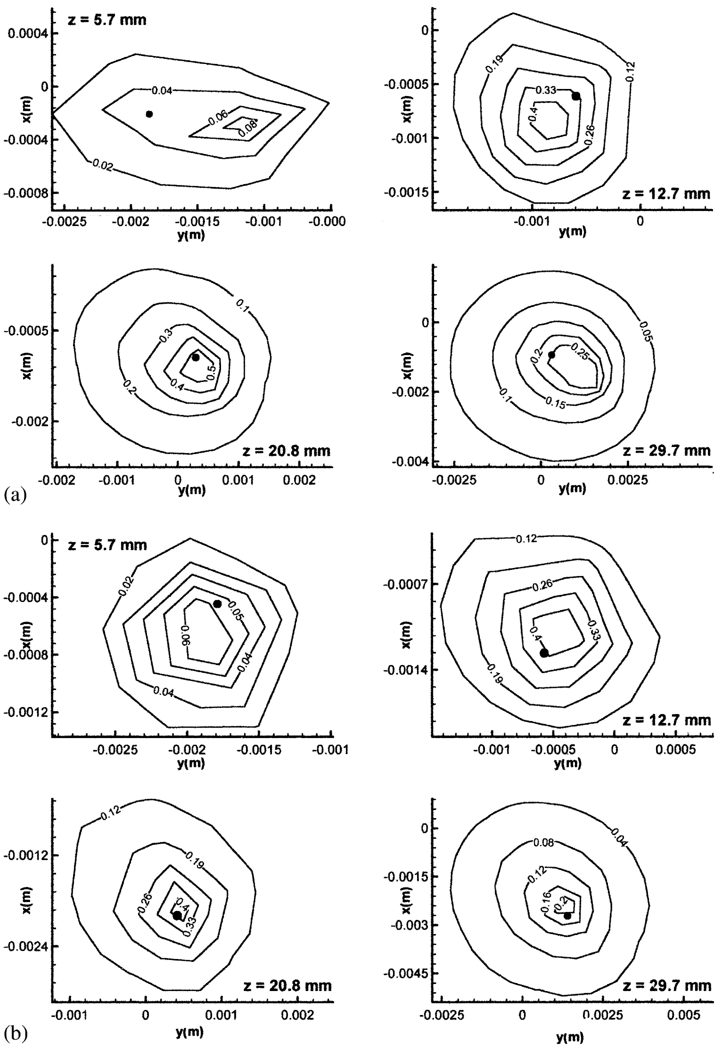

Fig. 7. Vapor mass concentration in the swirl plasma jet for different swirl velocities: (a) 20 and (b) 40 m s^{-1} (droplet loadings 600 g/h).

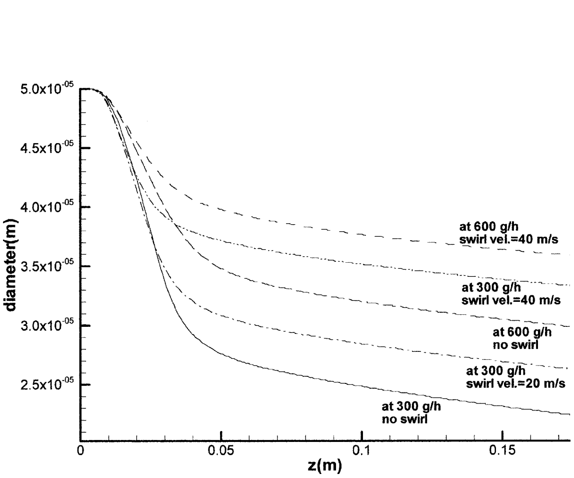

Fig. 8. Variation of the droplet size in the plasma jet.

evaporation, mixing effect is also plays an important role here. At $z = 39.3$ mm, the difference between the plasma temperature distributions with and without droplet loading can be negligible. This means that there is a negligible heat exchange between plasma and droplets in the downstream.

Fig. 10(a) and (b) are drawn for the plasma jet swirl velocity 20 and 40 m s^{-1} respectively at the droplet loading 600 g/h. It is clearly observed that increasing swirl velocity decreases the heat transfer from the plasma to the droplet, and the deflection of the plasma jet from the axis of the symmetry. If the swirl velocity is increased, the uniformity and broadness of radial distribution of the vapor concentration are increased. It indicates that swirl velocity improves the mixing of vapor with plasma. The results of Paik et al. [11] support same. Radial distribution of the vapor concentration at

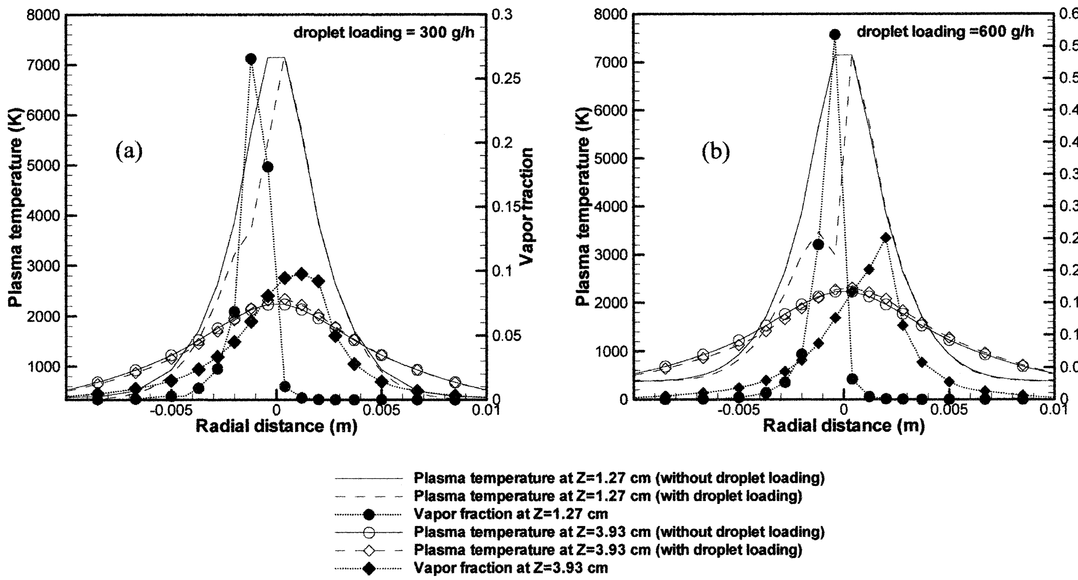

Fig. 9. Radial distribution of the non-swirl plasma jet temperature and vapor mass concentration for different droplet loadings: (a) 300 and (b) 600 g/h.

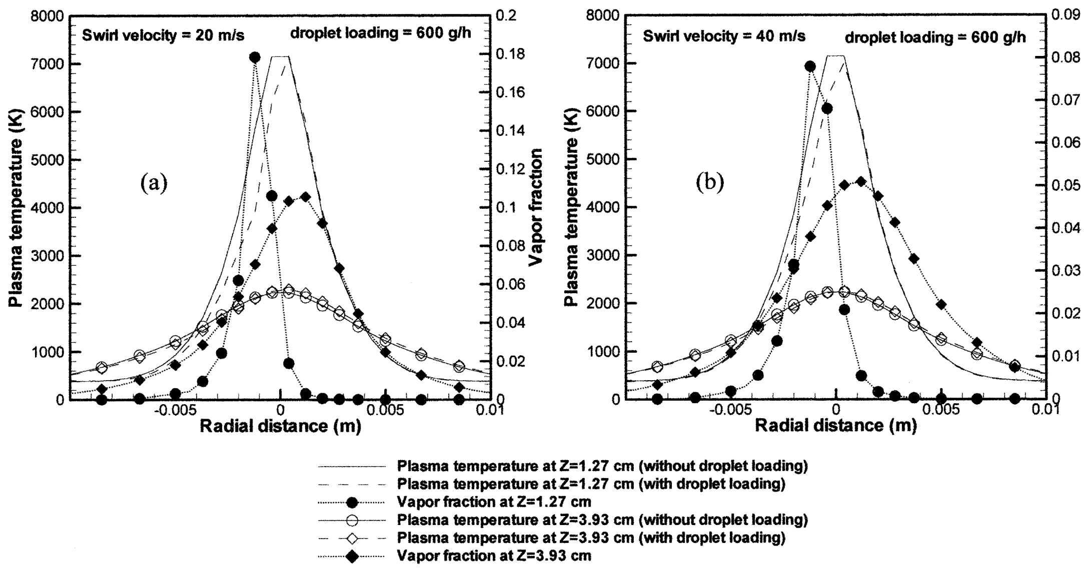

Fig. 10. Radial distribution of the swirl plasma jet temperature and vapor mass concentration for different swirl velocities: (a) 20 and (b) 40 $\mathrm{m\,s^{-1}}$ (droplet loadings 600 g/h).

$z = 39.3$ mm is more uniform and broader than the same at $z = 12.7$ mm in all cases. Hence it can be concluded that mixing of vapor with plasma is increased in the downstream direction.

The results of the temperature and vapor mass concentration fields predicted by this model are qualitatively similar to the experimental results [13].

5. Conclusion

3D effects of radial injection of water jet into both swirl and non-swirl Ar plasma jets are clarified under dense loading conditions by numerical simulation. A summary of results obtained by numerical model is as follows.

1. Higher droplet loading produces strong local deformation of the temperature and velocity fields of the plasma jet due to the strong interactions of droplets with plasma. The deformation of the both fields is relaxed in the downstream direction. Velocity fields are relaxed slower than temperature fields.
2. The shape of the vapor clouds is being changed as the shape of plasma jet fields in the downstream direction. Mass concentration of vapor is increased with increasing the droplet loading where as evaporation rate is decreased with increasing the droplet loading.
3. Mixing effect is stronger in downstream direction. Swirl velocity increases the mixing of vapor with plasma but decreases the evaporation rate.
4. The results of the temperature and vapor mass concentration fields predicted by this model are qualitatively similar to that of available experiment.

Acknowledgements

The present work was partly supported by the grant-in-aid for scientific research (B) (2) from Japan Society for Promotion of Science (2001). Authors acknowledge the data base support of Dr. Pavel Kotalik, Institute of Plasma Physics, Czech Republic.

References

[1] H. Zhu, Y.C. Lau, E. Pfender, Deposition of $Yba_2Cu_3O_{7-x}$ thick films by the spray ICP technique, In: Proceedings of Ninth International Symposium on Plasma Chemistry, Pugnochiuso, Italy, 1989, Vol. 3, pp. 1497–1502.
[2] M. Asmann, D. Kolman, J. Heberlein, E. Pfender, Experimental confirmation of thermal plasma CVD of diamond with liquid feedstock injection model, Diamond Relat. Mater. 9 (1) (2000) 13–21.
[3] H. Zhu, Y.C. Lau, E. Pfender, RF plasma synthesis of $Yba_2Cu_3O_{7-x}$ powders, J. Supercond. 3 (1) (1990) 171–175.
[4] J. Karthikeyan, C.C. Berndt, J. Tikkanen, S. Reddy, H. Herman, Plasma spray synthesis of nanomaterial powders and deposits, Mater. Sci. Eng. A 238 (2) (1997) 275–286.
[5] V. Yargeau, G. Soucy, M.I. Boulos, The treatment of water-based toxic waste using induction plasma technology, Plasma Chem. Plasma Processing 19 (3) (1999) 327–340.
[6] A.b. Murphy, T. McAllister, Modeling of the physics and chemistry of thermal plasma waste treatment, Phy. Plasmas 8 (5) (2001) 2565–2571.
[7] P. Proulx, J. Mostaghimi, M.I. Boulos, Plasma–particle interaction effects in induction plasma modeling under dense loading conditions, Int. J. Heat Mass Transfer 28 (7) (1985) 1327–1336.
[8] D.K. Das, R. Sivakumar, Modelling of the temperature and the velocity of ceramic powder particles in a plasma flame—I. Alumina, Acta Metall. Mater. 38 (11) (1990) 2187–2192.
[9] X. Chen, E. Pfender, Heat transfer to a single particle exposed to a thermal plasma, Plasma Chem. Plasma Processing 2 (2) (1982) 185–212.
[10] Y.P. Wan, V. Prasad, G.-X. Wang, S. Sampath, J.R. Fincke, Model and powder particle heating, melting, resolidification, and evaporation in plasma spraying processes, ASME J. Heat Transfer 121 (1999) 691–699.
[11] S. Paik, Xi. Chen, P. Kong, E. Pfender, Modeling of a counterflow plasma reactor, Plasma Chem. Plasma Processing 11 (2) (1991) 229–249.
[12] D. Kolman, J. Heberlein, E. Pfender, A three-dimensional two-phase model for thermal plasma chemical vapor deposition with liquid feedstock injection, Plasma Chem. Plasma Processing 18 (1) (1998) 73–89.
[13] K. Wittmann, J-F. Coudert, P. Fauchais, F. Blein, Study of the interaction of liquid jet and a DC plasma jet by optical emission spectroscopy, In: Proceedings of Fifteenth International Symposium on Plasma Chemistry, Orleans, France, 2001, Vol. 3, pp. 509–514.
[14] A. Vardelle, P. Fauchais, B. Dussoubs, N.J. Themelis, Heat generation and particle injection in a thermal plasma torch, Plasma Chem. Plasma Process 18 (1998) 551–554.
[15] M.I. Boulos, P. Fauchais, E. Pfender, Thermal Plasmas: Fundamentals and Applications, Vol. 1, Plenum, New York, 1994.
[16] M. Hrabovsky, P. Krenek, Properties of thermal plasma generated by the torch with water stabilized arc, In: Proceedings of Eleventh International Symposium on Plasma Chemistry, Loughborough, England, 1993, Vol. 1, p. 315–320.
[17] R. Bolot, C. Coddet, M. Imbert, The use of the phoenics code for plasma jet modeling, Phoenics J. Comp. Fluid Dyn. Appl. 10 (3) (1997) 335–352.
[18] H. Nishiyama, T. Saito, S. Kamiyama, Numerical simulation of a nonequilibrium plasma jet in an applied magnetic field using three-fluid model, Plasma Chem. Plasma Processing 16 (1996) 265–286.
[19] C.H. Chang, J.D. Ramshaw, Numerical simulations of argon plasma jets flowing into cold air, Plasma Chem. Plasma Processing 13 (1993) 189–209.
[20] R. Spores, E. Pfender, Flow structure of a turbulent thermal plasma jet, Surf. Coat. Technol. 37 (1989) 251–270.
[21] C.T. Crowe, M.P. Sharma, D.E. Stock, The particle-source-in cell (PSI-CELL) model for gas-droplet flows, ASME J. Fluids Eng. 99 (1977) 325–332.
[22] D.B. Spalding, Phoenics overview, CHAM, UK, 2000.
[23] E. Pfender, Particle behavior in thermal plasma, Plasma Chem. Plasma Processing 9 (1989) 167–S94.
[24] E. Pfender, Y.C. Lee, Particle dynamics and particle heat and mass transfer in thermal plasmas. Part I The motion of a single particle without thermal effects, Plasma Chem. Plasma Processing 5 (1985) 211–237.